Impact of oxygen interdiffusion on spin-to-charge conversion at nonmagnetic metal/Bi oxide interfaces

S. Sugimoto,[1] J. Uzuhashi,[1] S. Isogami,[1] T. Ohkubo,[1] Y. K. Takahashi,[1] S. Kasai,[1,2,*] and K. Hono[1]
[1]*Research Center for Magnetic and Spintronic Materials, National Institute for Materials Science (NIMS), 1-2-1 Sengen, Tsukuba 305-0047, Japan*
[2]*JST, PRESTO, 4-1-8 Honcho, Kawaguchi, Saitama 332-0012, Japan*

(Received 14 April 2019; revised manuscript received 18 June 2019; published 14 October 2019)

Spin-to-charge conversion at metal/oxide interfaces with stacked structures of permalloy/(Cu or Ag)/Bi_2O_3 were systematically investigated by using the spin-pumping technique and cross-sectional transmission electron microscopy. Although the transport measurement reproduced the results in previous studies, the interfacial structure of (Cu or Ag)/Bi_2O_3 was found to change depending on the crystalline orientation of the Cu or Ag underlayer. While the Ag/Bi_2O_3 stacks with Ag(111) had steep interfaces, the formation of a nanometer-scale Cu-O layer can be found in the Cu/Bi_2O_3 interface, which should be the main origin of the sign inversion of the conversion coefficients between Cu/Bi_2O_3 and Ag/Bi_2O_3. This study stresses the importance of nanostructure identification for discussing spin-to-charge conversions at metal/oxide interfaces.

DOI: 10.1103/PhysRevMaterials.3.104410

I. INTRODUCTION

Exploration of the conversion mechanism between spin and charge currents is the essence of modern spintronics for realizing novel devices using spin-orbit torque (SOT). Early works attributed the giant spin Hall effect (SHE) to the large spin-orbit interaction (SOI) in bulk [1,2]. However, more recent investigations have indicated the importance of interfacial phenomena. In the past decade, the Rashba-Edelstein effect (REE) received much interest as a possible mechanism for interfacial spin-to-charge conversion [3,4]. Given the existence of large SOI, Fermi contours show a finite spin-split dispersion between the up and down spin states. When an interfacial charge current flows in a two-dimensional (2D) electron gas, helical spin polarization is accompanied by an in-plane spin accumulation perpendicular to the applied charge current. This nonequilibrium spin accumulation further induces a finite spin current at the interface, resulting in charge-to-spin conversion through the REE. The reverse process, i.e., spin-to-charge conversion at the Fermi contour, is called the inverse REE (IREE), in an analogy with the inverse SHE (ISHE).

Because the REE originates from a virtual electric field applied at the Fermi contour [5], the field induced at the nonmagnetic metal (NM)/strong SOI insulator interface can feasibly substitute for a REE-type charge-to-spin conversion source close to the interface. Based on this idea, Karube *et al.* [6] recently demonstrated anomalously efficient conversions at several Cu/Bi_2O_3 interfaces. Tsai *et al.* [7] also reported that an NM/Bi_2O_3 heterostructure could be used to control interfacial electron distribution by tuning the difference between the work functions across the interface. However, using oxide at the conversion interface usually carries a risk of unintended material oxidization. An *et al.* [8] reported that the natural oxidization of Cu induced a finite spin torque in spite of the negligible SOI of Cu. Such enhancements in the effective conversion factor have also been reported for other heterostructures, including Pt/CoFeB and Pt/Co [9], W/CoFeB [10], and Ta/Pt/Co [11]. It should be therefore difficult to distinguish the oxidization effect and the inherent IREE at metal/oxide interfaces, especially only by transport measurements.

In this study, we investigate spin-to-charge conversion efficiency at NM/Bi_2O_3 interfaces systematically to understand the conversion process. We discuss our results from four viewpoints to systemize the possible effects of NM/Bi_2O_3 interfaces:

(i) The effect of the crystalline orientation at the interface, by depositing a Ta buffer layer (BL) beneath the heterostructures.

(ii) The NM dependence, by comparing the effects of Cu and Ag spacers.

(iii) The effect of Bi segregation at the interface, by inserting a Bi layer between the NM and Bi oxide.

(iv) The exact role of a capping Bi_2O_3 layer (CL), by replacing it with SiO_2.

The conversion efficiency at each interface was evaluated using the spin-pumping technique, in the manner of IREE conversion. We also performed atomic level structure analyses at the interfaces by using high-resolution scanning transmission electron microscopy (STEM), with energy-dispersive x-ray spectroscopy (EDS).

We observed uniquely large conversion efficiencies at Cu/Bi_2O_3, Ag/Bi_2O_3, and Ag/Bi interfaces, as perfect reproductions of previous transport measurements [6,7,12,13]. Signs of the conversion constants were inverted between Ag and Cu spacers: the largest negative value was observed at the Cu/Bi_2O_3 interface while the largest positive one was obtained at the Ag/Bi interface, where the largest spin splitting via

*Corresponding author: KASAI.Shinya@nims.go.jp

the IREE has been implied under (111) crystal orientation by using spectroscopic measurements [14]. The atomic level structure analyses have provided further insights of such nontrivial conversion mechanism at Bi_2O_3 including interfaces. Our Bi_2O_3 CLs formed amorphous Bi oxide (a-Bi-O) above the bottom polycrystalline ferromagnetic (FM) and NM layers without Ta BLs, while once Ta BLs were inserted, the bottom layers were strongly aligned along the fcc (111) direction, which further promoted partial crystallization of α-Bi_2O_3 at interfaces; however, the enhanced crystalline orientation resulted in a decreased conversion efficiency, indicating the limitations of the IREE model in transport measurements. Remarkably, significant O interdiffusion from Bi_2O_3 into Cu resulted in the formation of a Cu-O barrier at the interface. This study has revealed that the interfacial fine structure plays a more significant role in estimations of spin-to-charge conversion at NM/oxide interfaces than the choice of materials.

II. METHODS

All the multilayers were prepared on thermally oxidized silicon substrates in an ultrahigh vacuum chamber at a base pressure of 10^{-6} Pa at ambient temperature. We fabricated 16 different series of samples to respond to the tests required for filling all conditions from (i) to (iv). The base structure of our multilayer stacks was $Fe_{20}Ni_{80}$ (Py) (5 nm)/NM (Cu or Ag, 10 nm)/oxide capping layer (CL) (Bi_2O_3 or SiO_2). Film stacks with Ta (1 nm) underlayers were also prepared to examine the contribution of the (111) orientation to spin-charge conversion. We also examined the effect of inserting Bi (5 or 30 nm) between the NM and capping layers. All the metallic layers were deposited using radio frequency (RF) magnetron sputtering except for the Bi layer, which was deposited using an e-beam evaporator. The oxide capping layers were deposited by the e-beam evaporator from the stoichiometric sintered targets.

Figure 1 is a schematic illustration of the samples and measurement setup. Ferromagnetic resonance (FMR) in the Py layer was excited by using a waveguide placed 2 μm away from the sample to apply a perpendicular RF magnetic field, $h_{\rm rf}$. The sample had wire widths ranging from 2 μm to 12 μm. The spin current caused by FMR was injected into the interface and converted into an electric dc voltage, V, through the IREE. All measurements were performed at room temperature.

The vertical spin current density J_s, transferred from the Py layer to the NM/oxide interface, is scaled by the amplitude of $h_{\rm rf}$ [15,16] as illustrated in Fig. 1(a):

$$J_s = \frac{2e}{\hbar} \times \frac{\hbar G_{\rm eff}^{\uparrow\uparrow} \gamma^2 h_{\rm rf}^2}{8\pi\alpha_{\rm eff}^2} \left[\frac{4\pi M_s\gamma + \sqrt{(4\pi M_s\gamma)^2 + 4\omega^2}}{(4\pi M_s\gamma)^2 + 4\omega^2} \right], \tag{1}$$

where $\omega = 2\pi f$, M_s, γ, e, and $\hbar$ are the angular frequency, saturation magnetization, gyromagnetic ratio, elementary charge, and reduced Planck constant, respectively. The amplitude of J_s is characterized by the spin mixing conductance $G_{\rm eff}^{\uparrow\uparrow}$ [17,18] arising from the difference between the damping in the studied sample ($\alpha_{\rm eff}$) and the damping in a single reference layer (α_0):

$$G_{\rm eff}^{\uparrow\uparrow} = \frac{4\pi M_s t_F}{g\mu_B}(\alpha_{\rm eff} - \alpha_0), \tag{2}$$

where t_F, g, and μ_B are the thickness of the ferromagnetic layer, Landé factor, and Bohr magnetization, respectively. The converted charge current I_c is defined by a unit of 2D current density, j_c:

$$j_c = \frac{I_c}{w} = \frac{V}{wR}, \tag{3}$$

where w, V, and R are the width, the detected voltage, and the total resistance of the sample wire, respectively. The IREE-induced spin-to-charge conversion constant ($\lambda_{\rm IREE}$) is $\lambda_{\rm IREE} = j_c/J_s$ in units of length. $\lambda_{\rm IREE}$ can also be expressed in terms of the Rashba parameter α_R and the momentum relaxation time τ at the interface [19]: $\lambda_{\rm IREE} = \alpha_R\tau/\hbar$. However, an experimental estimation of α_R using this expression is not a trivial exercise. This is because a determination of τ for the metallic surface of Bi is difficult, unlike in the bulk [20]. In this study, we quantitatively evaluated IREE by using the conversion constant, $\lambda_{\rm IREE}$, instead of the Rashba parameter, α_R.

Thin foil specimens were prepared for STEM observations by using the lift-out technique with a focused ion beam (FEI Helios Nanolab 650). Microstructural characterization was performed using a transmission electron microscope (FEI Titan G2 80–200), with a high-resolution EDS element-mapping capability.

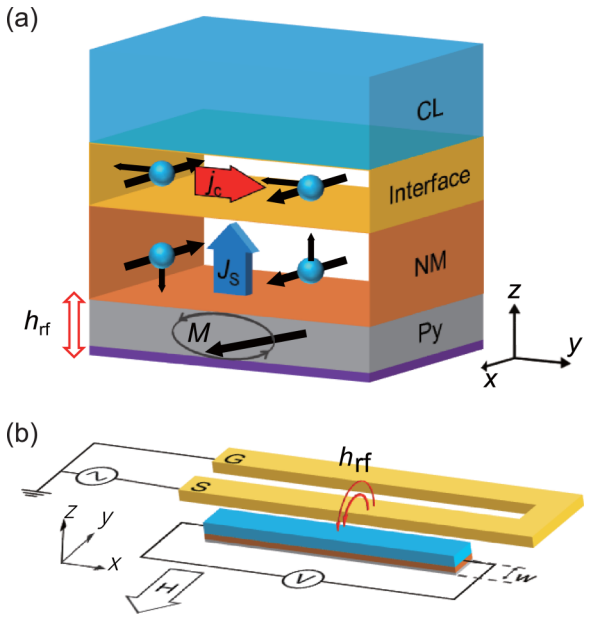

FIG. 1. (a) Schematic of spin-to-charge current conversion ascribed to the IREE. Spin currents are generated by spin pumping of the Py layer under FMR, travel through the NM layer, and reach the interface. Spin-to-charge current conversion occurs owing to spin-momentum locking at the interface between the NM layer and CL. (b) Schematic of the measurement setup.

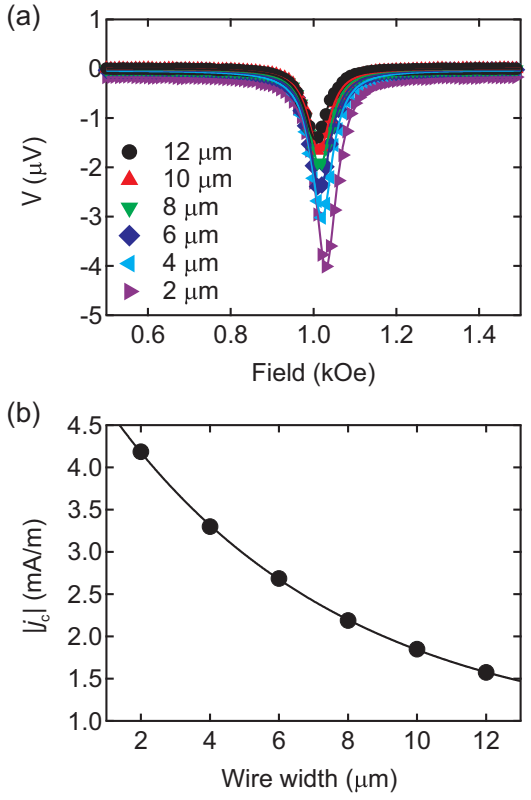

FIG. 2. (a) Resonance spectra of the rectified voltage V for different wire widths w of Py/Cu/Bi_2O_3 microwires. The excitation frequency $f = 9$ GHz. (b) The w dependence of the charge current density $|j_c|$. The solid curve is a fitting using an exponential decay curve.

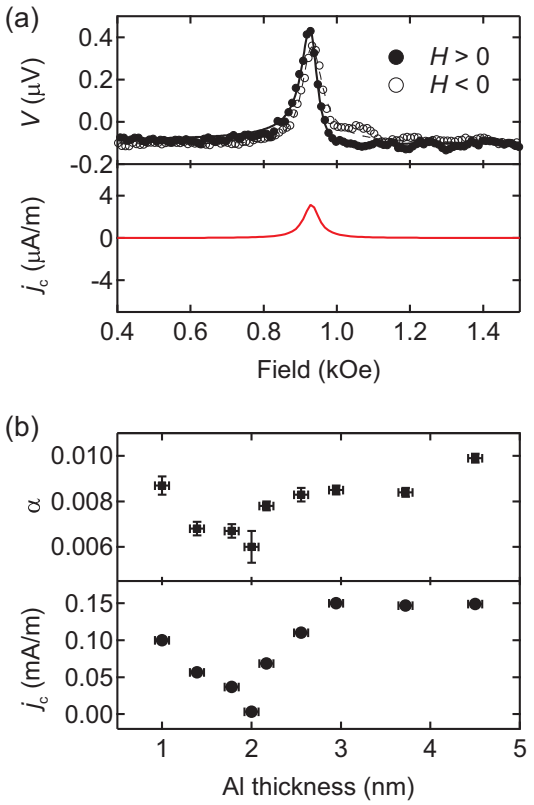

FIG. 3. (a) Resonance spectra of the rectified voltage V and the charge current density j_c, in Ta/Py/Al (2 nm). (b) Al thickness dependence of the Gilbert damping parameter α and charge current density j_c. The excitation frequency $f = 9$ GHz.

III. RESULTS AND DISCUSSION

First, the microfabricated device design was optimized. It should be noted that h_{rf} generated by a finite-scale waveguide is expected to have a nonuniform spatial distribution in the wired multilayers; i.e., the amplitude of h_{rf} becomes larger closer to the waveguide. Such an inhomogeneous h_{rf} triggers spatially nonuniform excitation of the FMR. Because λ_{IREE} scales with the gross area of the wire, as shown in Eq. (3), the spatial distribution of $h_{rf}(\mathbf{r})$ must be taken into account for the correct estimation of λ_{IREE}. Figure 2(a) shows the resonance spectra of the rectified V for various wire widths w, from 2 μm to 12 μm, measured at the Py/Cu/Bi_2O_3 microwire at 9 GHz. The monotonic decrease in the peak amplitude of V for wider samples indicates that h_{rf} may excite only one side of the wire edge, which would result in dissipative spin wave propagation along the y direction.

The width dependence of the evaluated charge current density amplitude, $|j_c|$, is plotted in Fig. 2(b). The experimental results follow an exponential decay curve, suggesting typical dissipative behavior along w. The attenuation length λ was estimated as $\lambda = 6.79 \pm 0.22$ μm, which was comparable with that of the magnetostatic surface spin wave of Py [21]. The other outcome from these results is the large scalability of $|j_c|$ against w. The value of $|j_c|$ when $w = 2$ μm is almost three times $|j_c|$ when $w = 12$ μm. Because $\lambda_{IREE} \propto |j_c|$, one also gets a 200% difference in conversion efficiency if the scale factor is not properly calibrated. Precise calibration requires knowledge of the spatial distribution of $h_{rf}(\mathbf{r})$, which appears in the injected current density J_s. Hereafter, all experimental results have been uniformly scaled with $w = 8$ μm, where values of $|j_c|$ at the Cu/Bi_2O_3 interface were scaled comparably with those of Ref. [6].

To discuss the effect of crystalline orientation on the IREE, detailed consideration for Ta/Py/NM structures should be necessary. These structures are known to form strong (111) orientation for Py and NM layers without epitaxial growth [22]. However, Ta possesses a large spin Hall angle (SHA) [23,24] so the ISHE signal at the Ta/Py interface should be evaluated in advance. We prepared Ta (1 nm)/Py (5 nm)/Al (t) trilayers, in which we continuously varied the Al layer thickness in the range of $0.0 \leqslant t \leqslant 5.0$ nm. The obtained resonance spectra for the ISHE voltage V and induced j_c, with $t = 2$ nm, are presented in Fig. 3(a). The solid and open symbols are plots of V under a positive field $H > 0$ and negative field $H < 0$, respectively. Finite resonance peaks were observed, but the sign-inverted ISHE component (the difference in voltage between the solid and open symbols) appeared very small, indicating that the Oersted-field-induced FMR excitation might be dominant. The ISHE components were quantified by fittings using a Lorentzian distribution and its derivative curves, and further converted into a charge current density, j_c, using Eq. (3). j_c remained on the order of μA/m, and more than 100 times smaller than those of

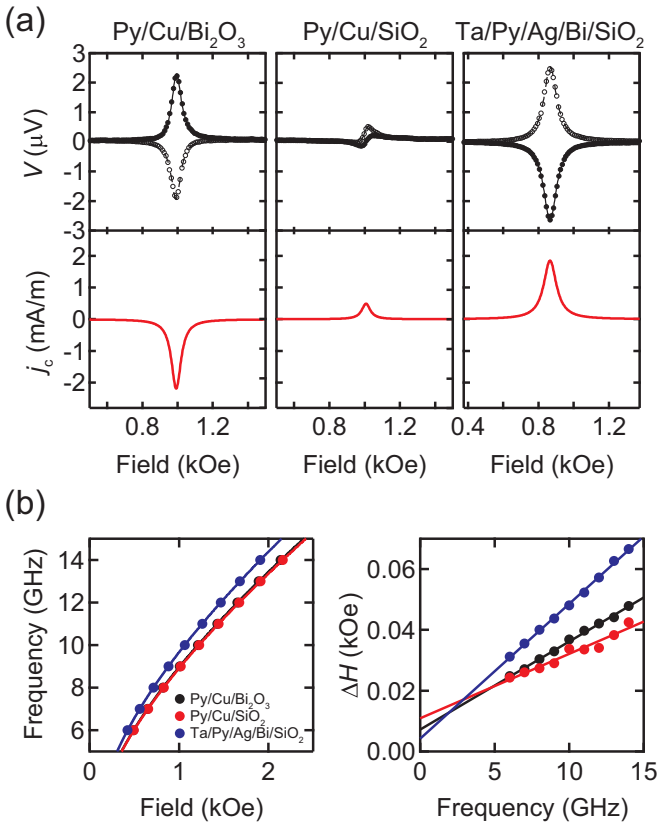

FIG. 4. (a) Resonance spectra for the rectified voltage V and charge current density j_c for $H > 0$ in various interfaces: (i) Py/Cu/Bi_2O_3, (ii) Py/Cu/SiO_2, and (iii) Ta/Py/Ag/Bi/SiO_2. Results for $H > 0$ are plotted as closed symbols, while those for $H < 0$ are plotted as open symbols. (b) Field dependencies of resonance frequencies in each interface. Solid curves indicate a fitting using the Kittel formula. (c) Frequency dependencies of FWHM ΔH for the spectrum at each interface. Solid lines are linear fittings.

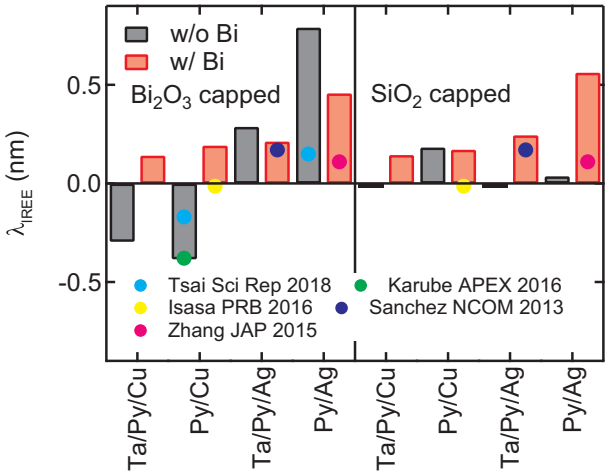

FIG. 5. Conversion efficiencies λ_{IREE} in various interfaces. Black bars indicate the results for the basic structures Ta/Py/NM (Cu or Ag)/CL (Bi_2O_3 or SiO_2), while red bars show the results of structures with Bi inserted between NM and CL. The solid colored circles indicate results from previous experiments which used the same spin-pumping techniques: Cu/Bi_2O_3 by Karube *et al.* [6], Cu/Bi_2O_3 and Ag/Bi_2O_3 by Tsai *et al.* [7], Ag(111)/Bi by Sánchez *et al.* [12], Ag/Bi by Zhang *et al.* [13], and Cu/Bi by Isasa *et al.* [20].

the Cu/Bi_2O_3 and Ag/Bi interfaces, as shown in Fig. 4(a). These results guarantee that the ISHE contribution at the Ta/Py interface is negligibly small in comparison to the signals from the NM/oxide interfaces. The origin of the small ISHE contribution can be explained by the large spin conductive mismatch between Py and the highly resistive, ultrathin Ta [25].

The dependencies of the damping constant, α, and j_c on the Al thickness t are shown in Fig. 3(b). The intrinsic damping constant, α, of FMR was evaluated from the frequency dependence of the full width at half maximum (FWHM) as $\Delta H = \Delta H_0 + (2\pi\alpha/\gamma)f$. These showed that the local minimum or maximum of α and j_c at $t = 2$ nm coincided. For thinner Al regions ($t < 2$ nm), the Py top surface was no longer protected by Al, and oxidization of Py enhanced the FWHM of Py FMR, which results in an apparent increase in α. For thicker Al regions ($t > 2$ nm), a Ta/Py/Al/Al-O multilayer formed owing to natural oxidization of Al. This may induce an additional rectified voltage at the Al/Al_2O_3 interface in the same manner as at the Cu/CuO interface [8]. Therefore, the value at $t = 2$ nm is expected to be the pure ISHE component at the Ta/Py interface. The referential damping constant $\alpha_0 = 0.006 \pm 0.001$ was also taken to deduce $G_{\text{eff}}^{\uparrow\uparrow}$, at this point.

Figure 4(a) shows the resonance spectra of the rectified V and the corresponding charge current density j_c for three different multilayers: Py/Cu/Bi_2O_3, Py/Cu/SiO_2, and Ta/Py/Ag/Bi/SiO_2. The symmetric peak and dip show clear sign inversion for $H > 0$ and for $H < 0$; this means that ISHE- and/or IREE-induced conversion signals were dominant here. The amplitude of the resonance signal appeared especially large in the Py/Cu/Bi_2O_3 and Ta/Py/Ag/Bi/SiO_2 samples, which indicated efficient spin-to-charge conversions at the Cu/Bi_2O_3 and Ag/Bi interfaces. Furthermore, the signs of j_c were different at these two interfaces, as reported previously [7]. The tiny signal obtained from the Py/Cu/SiO_2 sample is consistent with a finite ISHE due to Cu oxidization [8,26,27], although neither the Py/Cu nor the Cu/SiO_2 interfaces themselves possessed little SOI as freestanding structures. These results are perfect reproductions of the nonconventional interface spin-charge conversions at Cu/Bi oxide interfaces reported in Refs. [6,7]. The field dependence of the resonance frequency and the frequency dependence of FWHM ΔH have been plotted in Figs. 4(b) and 4(c). The results shown in Fig. 4(b) indicate that the resonance spectra could be attributed to a uniform Kittel mode, $f = 2\pi\gamma\sqrt{(H + H_c)(H + 4\pi M_s)}$, while those in Fig. 4(c) enabled us to evaluate the intrinsic damping constant, α, of the FMR for each sample.

Figure 5 summarizes λ_{IREE} for the 16 different samples measured at $f = 9$ GHz. The left panel shows the results for the samples with Bi_2O_3 capping layers, while the right panel indicates the samples with SiO_2 capping layers. The additional ISHE signal at the Ta/Py interfaces was calibrated from the results shown in Fig. 3. The insertion of the Ta BL improved (111) crystalline orientation of our Py/NM

polycrystals, as investigated by structure analysis below, whereas their conversion constants always decrease from those of noninserted samples in any combinations of spacers and CLs. Note that our samples with or without Ta BL possessed polycrystalline or polycrystalline-amorphous interfaces, as indicated in the latter structure analysis, differently from epitaxial interfaces used for angle-resolved photoemission spectroscopy (ARPES) measurements [14,28]. Our results clearly indicate that IREE tends to decrease under (111) crystalline orientation in polycrystalline and polycrystalline-amorphous interfaces, and further stress the importance of the nanostructure of realistic devices when discussing conversion efficiency.

The conversion phenomena exhibited the most dramatic changes at the interfaces including Bi_2O_3. Whereas the material dependencies of almost all of the NM/SiO_2 interfaces remained flat, and their $|\lambda_{IREE}|$ were small (about 0.01), the NM/Bi_2O_3 interfaces had λ_{IREE} values more than ten times larger (the black bars). Moreover, there were sign inversions between the Cu/Bi_2O_3 and Ag/Bi_2O_3, with and without the Ta BL [7]. These results clearly indicate that there was some kind of interfacial effect in the NM/Bi_2O_3 interfaces, and that it was not sensitive to the interfacial crystalline orientation. The origin of an unanticipated increase of the signal at Py/Cu/SiO_2 remains uncertain.

In the samples with a Bi insertion layer, the CL dependence was suppressed and λ_{IREE} turned out to have positive values for all of the interfaces (the red bars in the figures). This implies that the interfacial conversion physics were governed by the NM/Bi interfaces, rather than by the top CLs. In other words, Bi segregations at interfaces cannot be the origin of unique variations with Bi_2O_3 CL. There is strong debate on the SHE of Bi [29–31], and relevant estimation of the SHA for Bi only from the above results remains beyond our scope here.

The solid symbols show previously reported λ_{IREE}, which were measured using transport techniques, i.e., those of Cu/Bi_2O_3 by Karube *et al.* [6], Cu/Bi_2O_3 and Ag/Bi_2O_3 by Tsai *et al.* [7], Ag(111)/Bi by Sánchez *et al.* [12], Ag/Bi by Zhang *et al.* [13], and Cu/Bi by Isasa *et al.* [20]. Our results are comparable with these, showing particularly good agreement with those for Cu/Bi_2O_3 [6] and Ag(111)/Bi [12].

Because the REE is essential for the spin splitting of the Fermi contours, it was necessary to perform a precise structural analysis that directly correlated with the formation of the electrostatic potentials. Figure 6 shows the cross-sectional high-angle annular dark-field (HAADF) STEM images, and integrated nanobeam electron diffraction (NBD) patterns of the Bi_2O_3, NM (Cu or Ag), and Py layers in (a) Py/Cu/Bi_2O_3, (b) Py/Ag/Bi_2O_3, and (c) Ta/Py/Ag/Bi_2O_3. The cross-sectional images illustrate continuous and nonepitaxial growth of NM/oxide interfaces in all multilayers, and the NBD patterns provide details relating to film crystallinity.

The NBD patterns of the Bi_2O_3 layers all contain typical halo rings caused by the amorphous structure, indicating formations of as-deposited a-Bi-O layers, while NM and Py have spotted patterns unique to their crystalline structure. The

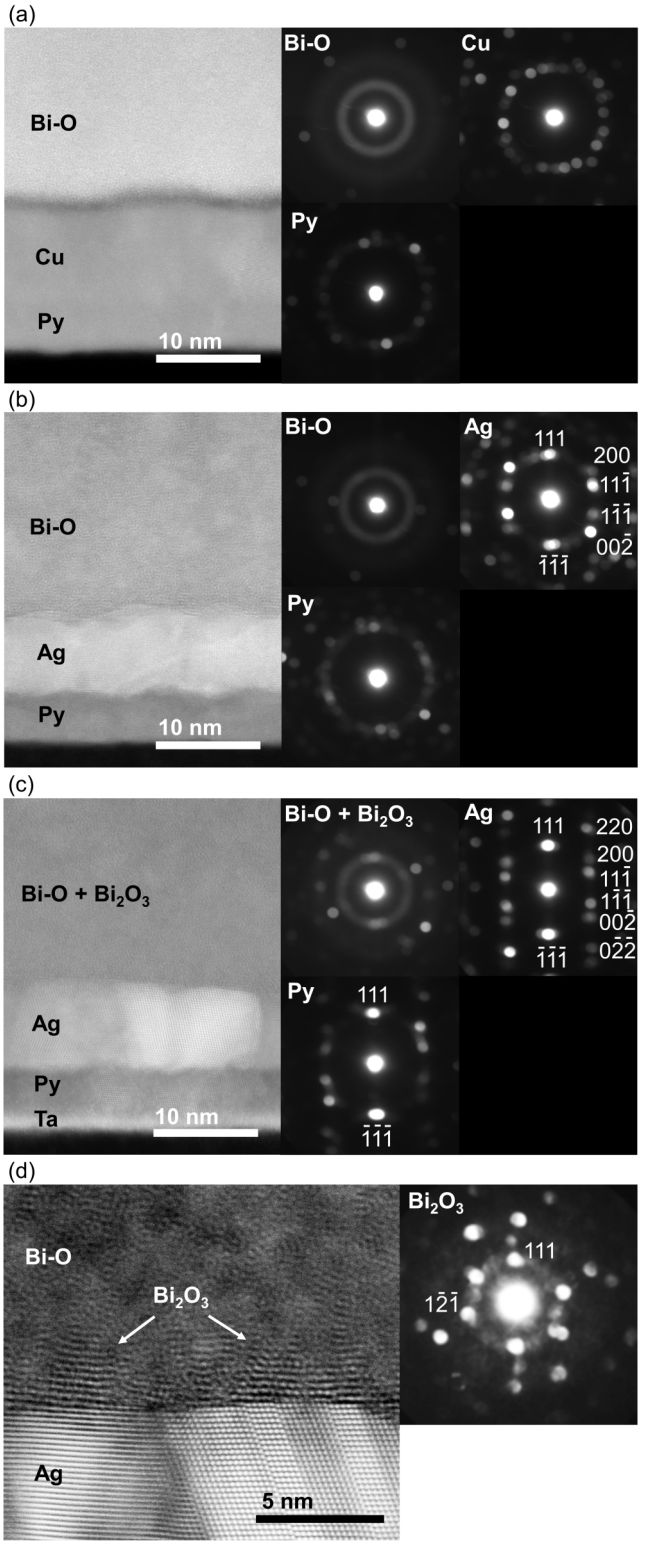

FIG. 6. Cross-sectional HAADF-STEM images and integrated NBD patterns for the Bi2O3, NM (Cu or Ag), and Py layers, in (a) Py/Cu/Bi_2O_3, (b) Py/Ag/Bi_2O_3, and (c) Ta/Py/Ag/Bi_2O_3. The NBD signals are integrated from 2 × 40 nm for Py, 5 × 40 nm for NM, and 10 × 40 nm for Bi_2O_3. (d) Magnified STEM image at Ag/Bi_2O_3 interface of (c) Ta/Py/Ag/Bi_2O_3. Inserted NBD signals are obtained at crystallized Bi_2O_3, as indicated by white arrows.

spotty patterns of NM and Py in Py/Cu/Bi_2O_3 [Fig. 6(a)] appear random, indicating that these layers have a nonoriented, polycrystalline nature. The diffraction pattern in the Ag layer of Py/Ag/Bi_2O_3 [Fig. 6(b)] and Ta/Py/Ag/Bi_2O_3 [Fig. 6(c)] is completely different: the (111) NBD spots appear much clearer, and NBD patterns of Ag and Py are identifiable along the [211], [110], and [$1\bar{1}0$] fcc zone directions. This crystalline orientation is further enhanced with Ta BL, which results in clear peaks in the XRD profiles (not shown). The crystallography remains polycrystalline, but its crystalline growth direction is strongly aligned to (111). Also, the halo ring of the a-Bi-O layer is switched to spotty patterns with Ta BL, corresponding to partial crystallization of Bi_2O_3 crystals there. Figure 6(d) shows the magnified STEM image of the Ag/Bi_2O_3 interface of Ta/Py/Ag/Bi_2O_3. Clear atomic columns are observed at the vicinity of the interface with Ag as shown by the arrows. NBD patterns obtained at these points [inset of Fig. 6(d)] are identifiable by monoclinic α-Bi_2O_3, the stable crystal of Bi_2O_3 at ambient conditions [32,33]. These results indicate that interface formations of Bi_2O_3-deposited NM are quite sensitive to crystalline orientations of bottom NMs, modified by insertions of Ta BLs, and further imply that the origin of unique variations in λ_{IREE} underneath the Bi_2O_3 CL in Fig. 5 can be ascribed to the difference in interfacial states, from nonoriented polycrystalline Cu/a-Bi-O to Ag(111)/α-Bi_2O_3.

Because Cu/Bi_2O_3 stacks are identified as polycrystalline-amorphous interfaces, the discussion provided in Ref. [7] on a freestanding α-Bi_2O_3 crystal turns out to be irrelevant to our situation. To get more concrete insights into NM/oxide interfaces, high-resolution STEM images, EDS elemental maps, and line profiles of each element of (a) Py/Cu/Bi_2O_3, (b) Py/Ag/SiO_2, (c) Py/Ag/Bi_2O_3, and (d) Ta/Py/Ag/Bi_2O_3 were prepared and have been presented in Fig. 7. It can be seen that almost all of the layers are well separated, and that steep interfaces form between Ta/Py, Py/NM, and NM/CL, independently of the NM and CL combination, although only the O layer of the Py/Cu/Bi_2O_3 sample diffused into the Cu layer [Fig. 7(a)]. Such nanoscale interdiffusion resulted in the formation of an insulating Cu-O barrier between the Cu/a-Bi-O interfaces, which appears as the dark contrast enclosed by the red dotted line in Fig. 7(a).

We next focus on line profiles of the elemental maps added to the right of the EDS maps. Here, the horizontal solid lines highlight the edge centers of each element (Bi, Si, O, Cu, and Ag) according to their fitted Boltzmann function. Nanometer-scale interdiffusion between O, Bi, and Cu was observed only at the Cu/Bi_2O_3 interface. The amplitude of the O interdiffusion was evaluated as a function of the distance between the O and Bi (Si) edge centers. Although the Cu/SiO_2 and Ag/Bi_2O_3 showed steep interfaces without any O interdiffusion, significant interdiffusion into the Cu layer was found in the case of Cu/Bi_2O_3. The depth reached 1.6 ± 0.1 nm which should not be treated as the fine 2D interface. These results indicate that the peculiar spin structure of the Bi_2O_3 alloy assumed in Ref. [7], discussed as the origin of large conversion efficiency, could be no longer maintained at the interfaces in the present samples. Or rather, our results are in agreement with recent observations of the interfacial Rashba SOT, in terms of oxygen incorporation.

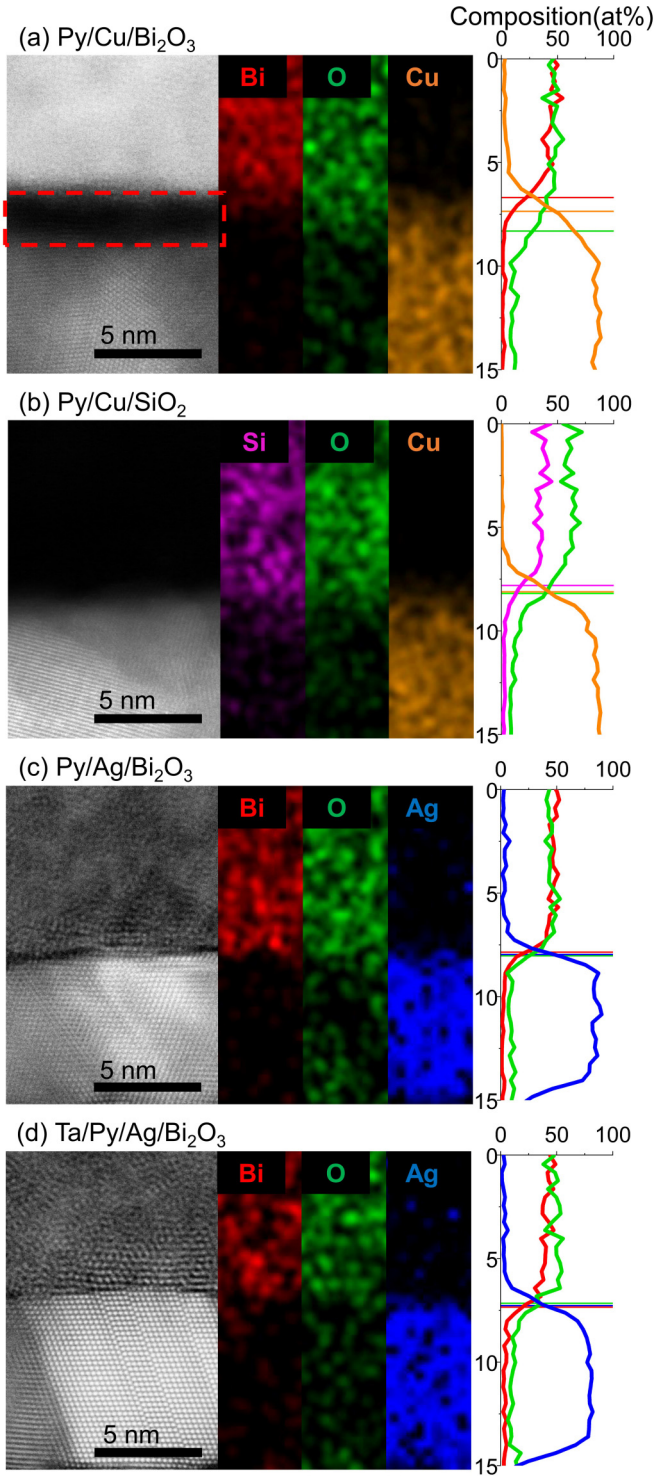

FIG. 7. High-resolution cross-sectional HAADF-STEM images at NM/oxide interfaces, and corresponding EDS maps for (a) Py/Cu/Bi_2O_3, (b) Py/Ag/SiO_2, (c) Py/Ag/Bi_2O_3, and (d) Ta/Py/Ag/Bi_2O_3. Line profiles of the elemental maps are plotted. Horizontal lines of the profiles exhibit edge centers for each element, obtained by Boltzmann function fittings.

To summarize all insights from the foregoing structure analysis with transport measurement, robust conditions of large anomalies in conversion at NM/Bi_2O_3 interfaces are

determined. First, large but inverted conversions at Cu/Bi_2O_3 are attributed to strong interdiffusion of oxygen from Bi_2O_3. Second, large conversions at Ag/Bi_2O_3 are attributed to neither the IREE at the Ag(111)/Bi interface nor the spin structure of the α-Bi_2O_3 crystal. A notable point is that the freestanding Bi_2O_3 alloy is not fundamental at any anomalies there. Further questions arise from these results, regarding the origin of the sign inversion at the O interdiffused Cu/Cu-O/a-Bi-O interface, and the enhanced λ_{IREE} at nonoriented Ag/Bi interfaces.

Very recently, Gao *et al.* [27] reported that the fieldlike SOT changed significantly, and even switched sign, when the interfacial oxidation level at Py/CuO_x bilayers was tuned. These results cannot directly compare with our ISHE and IREE signals obtained with the spin-pumping method, but underlying FM dynamics, which will affect spin current injection process also in our method, can be remarkably affected by Cu oxidization. We also refer to the orbital Hall effect (OHE) [34–36] predicted at several transition metals. Although no experimental observation of the OHE at any metallic heterostructure has been reported yet, such SOI-free angular momentum transfer may affect an increase in spin-to-charge conversions. Further systematic studies will be required to clarify the origin of the large charge current there.

The reasons for the λ_{IREE} at nonoriented Ag/Bi interfaces being larger than at Ag(111)/Bi interfaces in Fig. 5 are also nontrivial. In terms of fine-structure analysis, most previous reports on Ag/Bi interfaces using transport techniques [12,13] (including ours) could not claim to have achieved a perfect (111) crystalline orientation, because none had the required level of epitaxial flatness in ARPES [14]. Our study shows that the characteristics of Ag/Bi interfaces obtained in device structures should not be equivalently compared with those obtained ARPES measurements which reflect atomic level accuracy. That is, epitaxially grown Ag(111) might be required to make a precise comparison with the values of λ_{IREE} derived from transport measurements.

IV. CONCLUSION

In summary, the strong interfacial spin-to-charge conversion at NM (Cu or Ag)/Bi_2O_3 interfaces was comprehensively examined by spin-pumping measurements and atomic level structural analysis using HAADF-STEM imaging and EDS elemental mapping. We used four different criteria to distinguish bulky ISHE and interfacial IREE and revealed nontrivial effects from crystalline orientation and interfacial diffusion. Crystalline orientation significantly affects the interfacial formation when Bi_2O_3 is deposited on the NM layer. α-Bi_2O_3 is crystallized only when the bottom Ag layer is strongly aligned to the (111) direction while the nonoriented Cu layer results in amorphous Bi oxide at its interface. Also, no inherent increase but a small decrease in the IREE conversion efficiency is observed at the crystallized Ag(111)/α-Bi_2O_3 interface, compared with NM/a-Bi-O interfaces. These results imply the existence of extrinsic effects aside from interfacial contributions. Meanwhile, interfacial diffusion plays a crucial rule in the sign inversions observed at the Cu/Bi_2O_3 stack, forming the Cu/Cu-O/a-Bi-O interface, which could be ascribed to enhanced intrinsic SOT at the Cu-O insulating interlayer. These findings point to difficulties in comparing the results of transport measurements with those of surface ARPES measurements without an atomic level understanding of interfacial structure. Our work proposes a better understanding and engineering of efficient spin-to-charge interfacial conversion systems for future spintronic applications, through consideration of the interdiffusion between NM/Bi oxide interfaces.

ACKNOWLEDGMENTS

This work was partially supported by the Japan Society for the Promotion of Science, KAKENHI Grant No. 17K18892, and JST, PRESTO Grant No. JPMJPR18L3, Japan.

[1] M. I. Dyakonov and V. I. Perel, Phys. Lett. A **35**, 459 (1971).
[2] S. O. Valenzuela and M. Tinkham, Nature **442**, 176 (2006).
[3] Y. A. Bychkov and É. I. Rashba, Pis'ma Zh. Eksp. Teor. Fiz. **39**, 66 (1984) [JETP Lett. **39**, 78 (1984)].
[4] V. M. Edelstein, Solid State Commun. **73**, 233 (1990).
[5] S. E. Barnes, J. Ieda, and S. Maekawa, Sci. Rep. **4**, 4105 (2014).
[6] S. Karube, K. Kondou, and Y. Otani, Appl. Phys. Express **9**, 033001 (2016).
[7] H. Tsai, S. Karube, K. Kondou, N. Yamaguchi, F. Ishii, and Y. Otani, Sci. Rep. **8**, 5564 (2018).
[8] H. An, Y. Kageyama, Y. Kanno, N. Enishi, and K. Ando, Nat. Commun. **7**, 13069 (2016).
[9] X. Qiu, K. Narayanapillai, Y. Wu, P. Deorani, D.-H. Yang, W.-S. Noh, J.-H. Park, K.-J. Lee, H.-W. Lee, and H. Yang, Nat. Nanotechnol. **10**, 333 (2015).
[10] K.-U. Demasius, T. Phung, W. Zhang, B. P. Hughes, S.-H. Yang, A. Kellock, W. Han, A. Pushp, and S. S. P. Parkin, Nat. Commun. **7**, 10644 (2016).
[11] Y. Hibino, T. Hirai, K. Hasegawa, T. Koyama, and D. Chiba, Appl. Phys. Lett. **111**, 132404 (2017).
[12] J. C. R. Sánchez, L. Vila, G. Desfonds, S. Gambarelli, J. P. Attané, J. M. D. Teresa, C. Magén, and A. Fert, Nat. Commun. **4**, 2944 (2013).
[13] W. Zhang, M. Jungfleisch, W. Jiang, J. Pearson, and A. Hoffmann, J. Appl. Phys. **117**, 17C727 (2015).
[14] C. R. Ast, J. Henk, A. Ernst, L. Moreschini, M. C. Falub, D. Pacilé, P. Bruno, K. Kern, and M. Grioni, Phys. Rev. Lett. **98**, 186807 (2007).
[15] O. Mosendz, V. Vlaminck, J. E. Pearson, F. Y. Fradin, G. E. W. Bauer, S. D. Bader, and A. Hoffmann, Phys. Rev. B **82**, 214403 (2010).
[16] K. Ando, S. Takahashi, J. Ieda, Y. Kajiwara, H. Nakayama, T. Yoshino, K. Harii, Y. Fujikawa, M. Matsuo, S. Maekawa, and E. Saitoh, J. Appl. Phys. **109**, 103913 (2011).
[17] O. Mosendz, J. E. Pearson, F. Y. Fradin, G. E. W. Bauer, S. D. Bader, and A. Hoffmann, Phys. Rev. Lett. **104**, 046601 (2010).

[18] P. Gambardella and I. M. Miron, Philos. Trans. A: Math. Phys. Eng. Sci. **369**, 3175 (2011).
[19] K. Shen, G. Vignale, and R. Raimondi, Phys. Rev. Lett. **112**, 096601 (2014).
[20] M. Isasa, M. C. Martínez-Velarte, E. Villamor, C. Magén, L. Morellón, J. M. De Teresa, M. R. Ibarra, G. Vignale, E. V. Chulkov, E. E. Krasovskii, L. E. Hueso, and F. Casanova, Phys. Rev. B **93**, 014420 (2016).
[21] K. Yamanoi, S. Yakata, T. Kimura, and T. Manago, Jpn. J. Appl. Phys. **52**, 083001 (2013).
[22] R. Nakatani, K. Hoshino, S. Noguchi, and Y. Sugita, Jpn. J. Appl. Phys. **33**, 133 (1994).
[23] L. Liu, C.-F. Pai, Y. Li, H. W. Tseng, D. C. Ralph, and R. A. Buhrman, Science **336**, 555 (2012).
[24] M. Morota, Y. Niimi, K. Ohnishi, D. H. Wei, T. Tanaka, H. Kontani, T. Kimura, and Y. OtaniPhys. Rev. B **83**, 174405 (2011).
[25] G. Schmidt, D. Ferrand, L. W. Molenkamp, A. T. Filip, and B. J. van Wees, Phys. Rev. B **62**, R4790 (2000).
[26] R. Enoki, H. Gamou, M. Kohda, and J. Nitta, Appl. Phys. Exp. **11**, 033001 (2018).
[27] T. Gao, A. Qaiumzadeh, H. An, A. Musha, Y. Kageyama, J. Shi, and K. Ando, Phys. Rev. Lett. **121**, 017202 (2018).
[28] I. Gierz, B. Stadtmüller, J. Vuorinen, M. Lindroos, F. Meier, J. H. Dil, K. Kern, and C. R. Ast, Phys. Rev. B **81**, 245430 (2010).
[29] D. Hou, Z. Qiu, K. Harii, Y. Kajiwara, K. Uchida, Y. Fujikawa, H. Nakayama, T. Yoshino, T. An, K. Ando, X. Jin, and E. Saitoh, Appl. Phys. Lett. **101**, 042403 (2012).
[30] M. Matsushima, Y. Ando, S. Dushenko, and R. Ohshima, Appl. Phys. Lett. **110**, 072404 (2017).
[31] D. Yue, W. Lin, J. Li, X. Jin, and C. L. Chien, Phys. Rev. Lett. **121**, 037201 (2018).
[32] H. A. Harwig and Z. Anorg, Allg. Chem. **444**, 151 (1978).
[33] N. M. Sammes, G. A. Tompsett, H. Nafe, and F. Aldinger, J. Eur. Ceram. Soc. **19**, 1801 (1999).
[34] G. Y. Guo, Y. Yao, and Q. Niu, Phys. Rev. Lett. **94**, 226601 (2005).
[35] H. Kontani, T. Tanaka, D. S. Hirashima, K. Yamada, and J. Inoue, Phys. Rev. Lett. **100**, 096601 (2008).
[36] D. Go, D. Jo, C. Kim, and H.-W. Lee, Phys. Rev. Lett. **121**, 086602 (2018).